Optics Letters

# Large-scale silicon nitride nanophotonic phased arrays at infrared and visible wavelengths

Christopher V. Poulton,[1,*] Matthew J. Byrd,[1] Manan Raval,[1] Zhan Su,[1] Nanxi Li,[1,2] Erman Timurdogan,[1] Douglas Coolbaugh,[3] Diedrik Vermeulen,[1] and Michael R. Watts[1]

[1]Research Laboratory of Electronics, Massachusetts Institute of Technology, Cambridge, Massachusetts 02139, USA
[2]John A. Paulson School of Engineering and Applied Science, Harvard University, Cambridge, Massachusetts 02138, USA
[3]College of Nanoscale Science and Engineering, University at Albany, Albany, New York 12203, USA
*Corresponding author: cpoulton@mit.edu

Received 17 October 2016; revised 25 November 2016; accepted 27 November 2016; posted 28 November 2016 (Doc. ID 275446); published 20 December 2016

**We demonstrate passive large-scale nanophotonic phased arrays in a CMOS-compatible silicon photonic platform. Silicon nitride waveguides are used to allow for higher input power and lower phase variation compared to a silicon-based distribution network. A phased array at an infrared wavelength of 1550 nm is demonstrated with an ultra-large aperture size of 4 mm × 4 mm, achieving a record small and near diffraction-limited spot size of 0.021° × 0.021° with a side lobe suppression of 10 dB. A main beam power of 400 mW is observed. Using the same silicon nitride platform and phased array architecture, we also demonstrate, to the best of our knowledge, the first large-aperture visible nanophotonic phased array at 635 nm with an aperture size of 0.5 mm × 0.5 mm and a spot size of 0.064° × 0.074°.** 

***OCIS codes:*** (130.3120) Integrated optics devices; (250.5300) Photonic integrated circuits; (280.3640) Lidar.

https://doi.org/10.1364/OL.42.000021

Nanophotonic optical phased arrays have gained great interest in the last decade for applications such as LIDAR, free-space communication [1,2], image projection [3], and holographic displays [4]. Implementations in a custom silicon photonics platform [5], monolithically integrated electronics and photonics CMOS platform [6], a III-V hybrid platform [7], and within InP [8] have all been explored. Long-range power transmission for LIDAR or data-communication systems require beams from phased arrays to have a small diffraction angle, i.e., far field spot size, and high power. The former can be addressed with a larger aperture size and [9] has demonstrated a spot size of 0.14° × 0.14° at a wavelength of ∼1300 nm. The latter can be achieved with a higher input power on-chip. However, the nonlinearity-induced phase changes and material loss in silicon further limit the scalability and power output of silicon-based phased arrays.

Silicon nitride on silicon technology [10] has recently become a useful platform for silicon photonics, incorporating low-loss and fabrication-tolerant silicon nitride waveguides, silicon or germanium-based active components [1112], and rare-earth-ion-based optical amplifiers and lasers [13,14]. The low nonlinearity of silicon nitride [15] allows for the propagation of high guided optical power density [16], making it an ideal material for on-chip high-power distribution networks. Furthermore, silicon nitride waveguides have less fabrication-induced phase variation than silicon waveguides because of their lower index contrast which is beneficial for further scaling up the aperture size of a phased array. In addition, silicon nitride is also transparent at visible wavelengths [17,18], which enables potential applications of phased arrays in bathymetric LIDAR [19], optical trapping [20,21], and holography [4,22]. However, to the best of our knowledge, no large-scale silicon-nitride-based nanophotonic phased arrays have been demonstrated.

In this Letter, large-scale passive silicon-nitride-based optical phased arrays at infrared (IR) and visible wavelengths are demonstrated. Silicon nitride is used instead of silicon for its capability to handle high optical power and robustness to fabrication-induced phase variation. The demonstrated IR phased array operates at a wavelength of 1550 nm and has 1024 antennas, resulting in a 4 mm × 4 mm aperture size. To the best of our knowledge, this is the largest aperture nanophotonic phased array demonstrated to date and is an order of magnitude larger than prior demonstrated phased arrays [9]. This array is shown to be near diffraction-limited with a full width at half-maximum (FWHM) spot size of 0.021° × 0.021°. Due to the low nonlinearities of silicon nitride, we were able to transmit a 400 mW main beam with no noticeable nonlinearity-induced beam aberrations. In addition, with the transparency of silicon nitride at visible wavelengths, using the same fabrication process and design architecture, a phased array at a red wavelength of 635 nm was also demonstrated with an aperture size of 0.5 × 0.5 mm. To the best of our knowledge, this is the first large-aperture visible phased array and represents the first large-scale demonstration of "silicon photonics" within the visible spectrum.

A photograph of the demonstrated IR phased array is shown in Fig. 1(a). The phased array was fabricated at the CNSE in the SUNY Polytechnic Institute on a 300 mm silicon wafer with a 6 μm buried oxide using 193 nm immersion lithography.

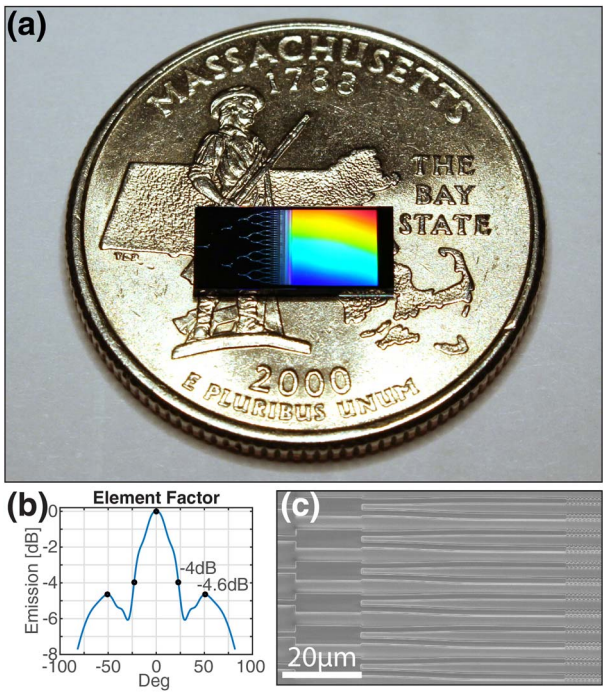


**Fig. 1.** (a) Photograph of the 4 mm × 4 mm IR phased array after fabrication. (b) Element factor of the antenna. (c) SEM image of the last stage of the splitter tree and antennas.

A 200 nm thick silicon nitride layer was deposited using a plasma-enhanced chemical vapor deposition process. The index of the silicon nitride film is 1.95. To couple 1550 nm light onto the chip, an on-chip inverse-taper edge coupler was designed to be matched with a 6.5 μm diameter mode from a lensed fiber. The phased array utilizes a binary tree distribution network of cascaded 1 × 2 multi-mode interference (MMI) splitters in order to distribute the input light to the antennas. Cascaded 1 × 2 splitters inherently result in a uniform amplitude and phase distribution to the antennas without any active tuning or passive delay lines.

Since the 1 × 2 splitter is cascaded for many stages, the efficiency of the splitter is an important figure of merit. A relatively large, highly efficient MMI splitter was designed for the beginning stages. However, due to the small pitch of the antennas (~4 μm), a smaller MMI splitter was required for the last stage of the tree to minimize evanescent crosstalk. Both MMI splitters were designed rigorously with finite-difference time-domain (FDTD) simulations. The larger MMI splitter consists of a 28.7 μm × 7 μm multi-mode region with 2.5 μm wide waveguide inputs and outputs. FDTD simulations of the larger MMI splitter design show a 0.04 dB insertion loss at the design wavelength of 1550 nm and a 0.1 dB bandwidth of over 100 nm showing the capability for a broadband distribution network. Utilizing an unbalanced tree, the insertion loss at 1550 nm is measured to be less than 0.1 dB. The smaller MMI splitter in the last stage of the tree is a 16 μm × 5 μm multi-mode region with 1.5 μm wide waveguide inputs and outputs. The simulated and measured insertion losses of this device are 0.27 and 0.35 dB, respectively.

The binary tree distribution network of the device pictured in Fig. 1(a) has 10 MMI splitter tree stages, giving a total count of 1024 antennas. The pitch of the antennas after the tree was 4 μm in order to minimize coupling between elements while maintaining a tight spacing. The uniform 4 μm pitch produces grating lobes at ±23° and ±51°. The reduction of this pitch is limited by evanescent coupling between antenna elements. The antenna was created by fabricating uniform inward symmetric 70 nm perturbations in the 1.5 μm wide waveguide. The antenna was designed to emit near 0° (perpendicular to the chip) in the antenna dimension at an input wavelength of 1550 nm. Antennas with a length of 4 mm were designed, giving a total phased array aperture of 4 mm × 4 mm. Figure 1(b) shows the element factor of the antenna. A scanning electron microscope (SEM) image of a portion of the last stage of the splitter tree and the antennas in a similar device is shown in Fig. 1(c).

Light at 1550 nm was input into the device with a 6.5 μm spot diameter lensed fiber. Figure 2(a) shows the resulting main beam on an IR card, and Fig. 2(b) shows an InGaAs IR camera image when the camera is directly placed in the path of the main beam at 0.05 m from the phased array. The main beam is clean with no noticeable light on the side which indicates that the binary tree distribution network has minimal phase variation. Here, the beam is relatively square because it has only propagated a short distance. The Fraunhofer distance of this array is 20 m so a sinc distribution is not expected at this distance. After a propagation distance of 10 m, the beam closer represents a sinc function [Fig. 2(c)]. Even after a propagation of 10 m, the beam has not increased greatly in size due to the large aperture of the phased array. The physical FWHM beam size after 10 m is 3.4 mm. This is similar to a Fresnel propagation simulation of a 4 mm × 4 mm uniform electric field propagating 10 m, which results in a 3.2 mm FWHM beam size. Fresnel propagation simulations are provided in the insets

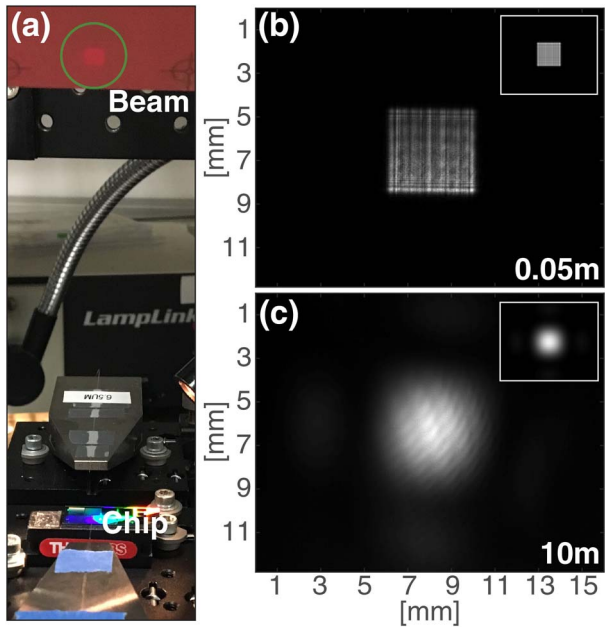


**Fig. 2.** (a) Photograph of the main beam of the array on an IR card. Main beam intensity measurement after approximately (b) 0.05 m and (c) 10 m of propagation. The insets show Fresnel propagation simulations in the same domain.

of Figs. 2(b) and 2(c), showing good agreement with the experimental measurements.

The far field of the array was measured with an InGaAs IR camera and a two-lens imaging system [9], and is shown in Fig. 3(a). A sinc function is observed in both the antenna and the array dimensions, which is expected for a near diffraction-limited square aperture. This indicates that little phase variation was accumulated in the silicon nitride tree and that the antenna elements were nearly identical. The FWHM spot size of the array was measured to be 0.021° × 0.021°, whereas the theoretical diffraction-limited spot size is 0.019° × 0.019°. This ultra-small spot size is over an order of magnitude smaller in area than the previous demonstration in [9] and allows for long-range propagation. For context, after 100 m of propagation, the diameter of the beam should increase by only 3.7 cm based on the experimental spot size. The intensity cuts of the spot along the array, $\theta$, and antenna, $\phi$, dimensions are shown in Fig. 3(b). Multiple side lobes are observed at the expected theoretical angular locations. A side lobe suppression of about 10 dB is measured. The −17 dB background noise level is caused by ambient radiation to the imaging system and is present without any input to the phased array.

The optical power of the main beam was measured by placing an InGaAs-integrating sphere photodiode directly in the path of the beam. The sphere was placed about 0.5 m away to ensure that the power within the grating lobes did not interfere with the measurement. The maximum power measured in the main beam was 400 mW with a power at the input fiber facet of 9.1 W, giving an overall efficiency of −13.6 dB. This efficiency can be decomposed into the fiber-to-chip coupling loss (2.8 dB), the MMI splitter tree network loss (1.3 dB MMI loss and 0.5 dB linear loss), and the antenna emission loss (9 dB). Specifically, the presence of the grating lobes causes 4 dB of the 9 dB antenna emission loss.

Since the demonstrated phased array was fabricated in silicon nitride, the same architecture can be utilized for visible wavelengths. A phased array was designed for a red wavelength of 635 nm. For the splitter distribution network, 400 nm wide (200 nm thick) single-mode waveguides were used for routing. The MMI splitters consisted of a 7.5 μm × 2.24 μm multimode region with 800 nm wide inputs and outputs. For this tree, only a single MMI splitter size was needed for a 2 μm antenna pitch. Using FDTD, the insertion loss of the MMI splitter was simulated to be 0.03 dB at a wavelength of 635 nm. The antennas were realized similarly to the IR antennas with inward symmetric perturbations in the waveguide. Light was input into this array with a cleaved SM600 fiber incident on an inverse-taper edge coupler designed to be matched to the fiber mode.

Figure 4(a) is a visible camera image of a 0.5 mm × 0.5 mm visible phased array when 635 nm light is input into the chip. The input laser power was increased intentionally in order to see the effect of wave guiding and MMI splitter scattering, clearly showing the MMI splitter tree architecture. However, this input power level saturated the camera, causing the array region to appear white. Figure 4(b) shows the output of the array on a white card. Five red spots are clearly seen. Two additional spots emitting at ±73° due to the 2 μm antenna pitch are not shown on the card. A small amount of light is observed between the spots, showing that the binary tree distribution network has a noticeable amount of phase variation.

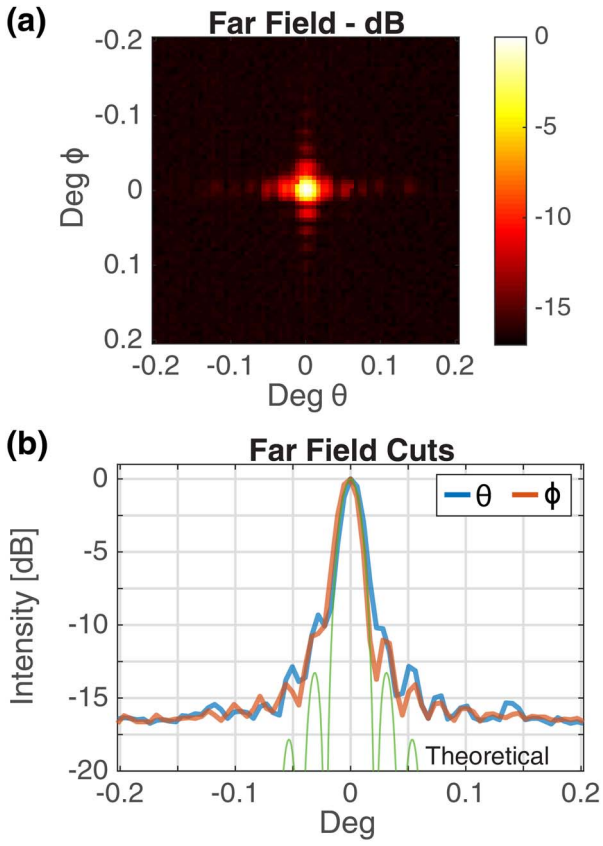


**Fig. 3.** (a) Far field of the main beam of the IR phased array on a log scale. (b) Far field intensity cuts of the phased array along the array, $\theta$, and antenna, $\phi$, dimensions.

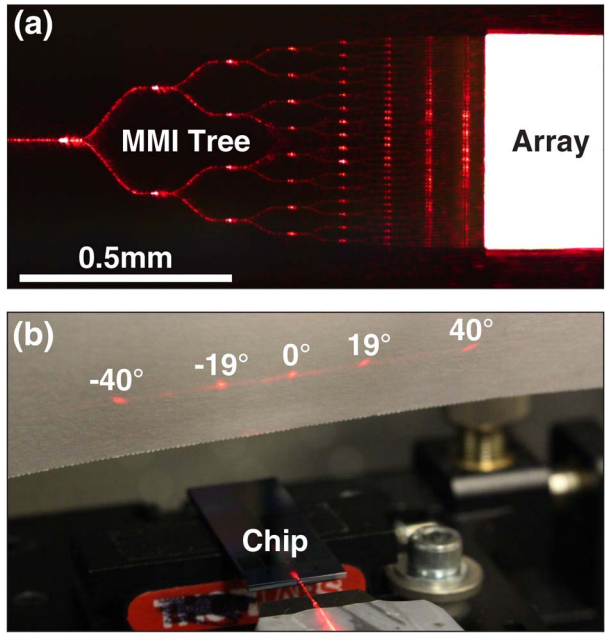


**Fig. 4.** (a) Saturated visible image of the 635 nm 0.5 mm × 0.5 mm phased array. (b) Photograph of the visible phased array output on a white card.

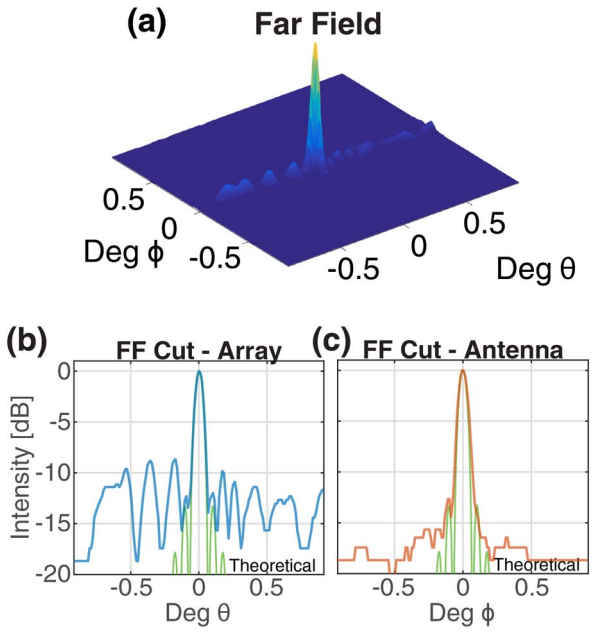


**Fig. 5.** (a) Far field of the visible array. (b) Far field intensity cuts of the visible phased array along the array, $\theta$, and (c) antenna, $\phi$, dimensions.

Using a similar two-lens imaging system as that of the IR array, the measured far field of the main beam of the visible array is shown in Fig. 5(a). A clear spot is observed with strong side lobes shown in the array dimension. The measured FWHM spot size was $0.064° \times 0.074°$, whereas $0.063° \times 0.063°$ is the theoretical diffraction limit of the square aperture. The increase of the spot size in the antenna dimension compared to the diffraction limit is expected due to the designed exponential emission pattern of the antennas instead of a uniform emission pattern. A side lobe suppression of 8.7 dB is measured in the array dimension. Multiple strong side lobes are observed, indicating the presence of phase variation in the splitter tree. This is most likely due to side-wall roughness that interacts with the more confined visible waveguide mode. Designing the array for a TM-polarized input could minimize the interaction with the side-wall roughness.

In conclusion, large-scale phased arrays based on silicon nitride have been demonstrated at IR and visible wavelengths. The phased arrays utilize a binary tree distribution network with cascaded $1 \times 2$ MMI splitters. The use of silicon nitride allowed for a low phase variation distribution network as seen by the demonstrated near diffraction-limited 4 mm × 4 mm phased array. To the best of our knowledge, this phased array is the largest aperture to date by over an order of magnitude. A main beam spot size of $0.021° \times 0.021°$ was measured with a side lobe suppression of 10 dB and a 400 mW main beam output. This demonstration shows the scalability of optical phased arrays, and the diffraction-limited performance indicates that even larger apertures are possible. Future work in silicon nitride on silicon platforms can utilize the demonstrated distribution network followed by a transition to a silicon layer for element phase shifting. The silicon nitride platform also enabled the demonstration of a phased array at a visible wavelength of 635 nm. An aperture size of 0.5 mm × 0.5 mm was shown with a spot size of $0.064° \times 0.074°$. To the best of our knowledge, this phased array is the first of its kind and shows that large-scale silicon-nitride-based photonics is possible at visible wavelengths.

**Funding.** Defense Advanced Research Projects Agency (DARPA) (HR0011-12-2-0007).

**Acknowledgment.** The authors thank Dr. Joshua Conway for helpful discussions. N. Li acknowledges a fellowship from the Agency of Science, Technology and Research (A*STAR), Singapore.

## REFERENCES

1. W. S. Rabinovich, P. G. Goetz, M. Pruessner, R. Mahon, M. S. Ferraro, D. Park, E. Fleet, and M. J. DePrenger, Proc. SPIE **9354**, 93540B (2015).
2. B. Guan, R. P. Scott, C. Qin, N. K. Fontaine, T. Su, C. Ferrari, M. Cappuzzo, F. Klemens, B. Keller, M. Earnshaw, and S. J. B. Yoo, Opt. Express **22**, 145 (2014).
3. F. Aflatouni, B. Abiri, A. Rekhi, and A. Hajimiri, Opt. Express **23**, 21012 (2015).
4. M. Raval, A. Yaacobi, D. Coleman, N. M. Fahrenkopf, C. Baiocco, G. Leake, T. N. Adam, D. Coolbaugh, and M. R. Watts, in *IEEE Photonics Conference* (2016), paper MG3.4.
5. A. Yaacobi, J. Sun, M. Moresco, G. Leake, D. Coolbaugh, and M. R. Watts, Opt. Lett. **39**, 4575 (2014).
6. H. Abediasl and H. Hashemi, Opt. Express **23**, 6509 (2015).
7. J. Hulme, J. Doylend, M. Heck, J. Peters, M. Davenport, J. Bovington, L. Coldren, and J. Bowers, Opt. Express **23**, 5861 (2015).
8. W. Guo, P. R. Binetti, C. Althouse, M. L. Mašanović, H. P. Ambrosius, L. A. Johansson, and L. A. Coldren, IEEE J. Sel. Top. Quantum Electron. **19**, 8500508 (2013).
9. D. N. Hutchison, J. Sun, J. K. Doylend, R. Kumar, J. Heck, W. Kim, C. T. Phare, A. Feshali, and H. Rong, Optica **3**, 887 (2016).
10. W. D. Sacher, Y. Huang, G.-Q. Lo, and J. K. S. Poon, J. Lightwave Technol. **33**, 901 (2015).
11. L. Chen, C. R. Doerr, L. Buhl, Y. Baeyens, and R. A. Aroca, IEEE Photon. Technol. Lett. **23**, 869 (2011).
12. L. Chen, C. R. Doerr, P. Dong, and Y. K. Chen, Opt. Express **19**, B946 (2011).
13. Purnawirman, J. Sun, T. N. Adam, G. Leake, D. Coolbaugh, J. D. B. Bradley, E. S. Hosseini, and M. R. Watts, Opt. Lett. **38**, 1760 (2013).
14. J. D. B. Bradley, E. S. Hosseini, Purnawirman, Z. Su, T. N. Adam, G. Leake, D. Coolbaugh, and M. R. Watts, Opt. Express **22**, 12226 (2014).
15. K. Ikeda, R. E. Saperstein, N. Alic, and Y. Fainman, Opt. Express **16**, 12987 (2008).
16. D. T. H. Tan, K. Ikeda, P. C. Sun, and Y. Fainman, Appl. Phys. Lett. **96**, 061101 (2010).
17. A. Subramanian, P. Neutens, A. Dhakal, R. Jansen, T. Claes, X. Rottenberg, F. Peyskens, S. Selvaraja, P. Helin, B. Du, Bois, K. Leyssens, S. Severi, P. Deshpande, R. Baets, and P. Van, Dorpe, IEEE Photon. J. **5**, 2202809 (2013).
18. W. Stutius and W. Streifer, Appl. Opt. **16**, 3218 (1977).
19. C.-K. Wang and W. D. Philpot, Remote Sens. Environ. **106**, 123 (2007).
20. K. K. Mehta and R. J. Ram, "Precise and diffraction-limited waveguide-to-free-space focusing gratings," arXiv 1607.00107 (2016).
21. E. R. Dufresne and D. G. Grier, Rev. Sci. Instrum. **69**, 1974 (1998).
22. D. Fattal, Z. Peng, T. Tran, S. Vo, M. Fiorentino, J. Brug, and R. G. Beausoleil, Nature **495**, 348 (2013).